

## A model of the lateral line of fish for vortex sensing

This article has been downloaded from IOPscience. Please scroll down to see the full text article.

2012 Bioinspir. Biomim. 7 036016

(<http://iopscience.iop.org/1748-3190/7/3/036016>)

View [the table of contents for this issue](#), or go to the [journal homepage](#) for more

Download details:

IP Address: 128.227.50.160

The article was downloaded on 22/05/2012 at 03:23

Please note that [terms and conditions apply](#).

# A model of the lateral line of fish for vortex sensing

Zheng Ren<sup>1</sup> and Kamran Mohseni<sup>1,2,3,4</sup>

<sup>1</sup> Department of Mechanical and Aerospace Engineering, University of Florida at Gainesville, FL 32611-6250, USA

<sup>2</sup> Department of Electrical and Computer Engineering, University of Florida at Gainesville, FL 32611-6250, USA

<sup>3</sup> Institute for Networked Autonomous Systems, University of Florida at Gainesville, FL 32611-6250, USA

E-mail: [mohseni@ufl.edu](mailto:mohseni@ufl.edu)

Received 23 September 2011

Accepted for publication 12 March 2012

Published 15 May 2012

Online at [stacks.iop.org/BB/7/036016](http://stacks.iop.org/BB/7/036016)

## Abstract

In this paper, the lateral line trunk canal (LLTC) of a fish is modeled to investigate how it is affected by an external flow field. Potential flow theory is adopted to model the flow field around a fish's body in the presence of a Karman vortex street. Karman and reverse Karman streets represent the flow patterns behind a bluff body and a traveling fish, respectively. An analytical solution is obtained for a flat body, while a fish-like body is modeled using a Joukowski transformation and the corresponding equations are solved numerically. The pressure distribution on the body surface is then computed employing Bernoulli's equation. For a known external flow, the flow inside the LLTC is driven by the pressure gradient between a pair of consecutive pores, which can be solved analytically. Governing dimensionless parameters are obtained from this analytical solution, and the effects of these numbers on the amplitude or features of the velocity distribution inside the canal are studied. The results show that the main characteristics of a vortex street including the magnitude of vortices, their translational speed, their spacing, their distance from the fish's body and the angle of the vortex street axis can all be recovered by measuring the velocity distribution along the canal and its changes with time. To this end, the proposed LLTC model could explain how a fish identifies the characteristics of a Karman vortex street shed by a nearby object or a traveling fish. It is also demonstrated that while this model captures the ac (alternating current) component of the external velocity signal, the dc (direct current) component of the signal is filtered out. Based on the results of our model, the role of the LLTC in a fish's schooling and its evolutionary impact on fish sensing are discussed.

(Some figures may appear in colour only in the online journal)

## Nomenclature

$a$	Radius of cylinder	$d, d^*$	Diameter of lateral line canal, and its dimensionless form
$b$	Vertical distance between vortices	$h, h^*$	Vertical distance between fish and vortex street, and its dimensionless form
$c, c^*$	Chord length of fish's body, and its dimensionless form	$l$	Horizontal distance between vortices
$c_0$	Coefficient of Joukowski transformation	$L$	Length of lateral line
		$P_0$	Total pressure at far field
		$P_L$	Pressure at left end of pipe
		$P_R$	Pressure at the right end of pipe

<sup>4</sup> Author to whom any correspondence should be addressed.

$P_{\text{surf}}$	Pressure on the flat plate surface
$r$	Radius in cylindrical coordinate
$t, t^*$	Time and its dimensionless form
$u$	Velocity component in the $x$ direction
$u_c$	Flow velocity inside canal
$u_s$	Velocity of vortex street
$U_\infty$	Free stream velocity at infinity
$U_{\text{tr}}$	Velocity of vortex street in static fluid
$v$	Velocity component in the $y$ direction
$V_{\text{in}}$	Characteristic velocity inside lateral line canal
$V_{\text{surf}}$	Velocity on the flat plate surface
$W$	Complex potential
$x, x^*$	Coordinates along the fish's body axis, and its dimensionless form
$z$	Complex coordinates after Joukowski transformation
$\Gamma, \Gamma^*$	Circulation strength of vortex, and its dimensionless form
$\delta$	Thickness of fish-like body
$\Delta L$	Distance between adjacent pores in lateral line
$\zeta$	Complex coordinates before Joukowski transformation
$\zeta_n, \bar{\zeta}_n$	Coordinate of vortex in the $\zeta$ -plane, and its complex conjugate
$\theta$	Angle between the vortex street axis and fish's body
$\lambda$	Thickness ratio of fish-like body
$\mu$	Dynamic viscosity of fluid inside canal
$\nu, \nu^*$	Kinetic viscosity of fluid inside canal, and its dimensionless form
$\Pi$	Dimensionless velocity inside lateral line canal
$\rho$	Density of external fluid
$\phi$	Velocity potential
$\psi$	Stream function
$\omega$	Angular velocity
$\omega_D^*$	Kinetic Reynolds number

## 1. Introduction

Fish possess a mechanosensory lateral line system, which responds to the motion of the surrounding water relative to the fish's skin. This sensing system could consist of a superficial neuromast (SN) and a canal neuromast (CN) subsystems. SNs are located on the outer surface of a fish, extending into the external fluid, while CNs are buried inside the lateral line canal (see figure 1). The basic sensing unit of the two is the fish's hair cell. Such hair cells will deflect as the result of oncoming flow, thus allowing for detection. SNs are generally smaller in diameter but greater in height than CNs and contain fewer hair cells [1]. Research on the lateral line has shown that SNs respond to changes in external flow velocity, whereas CNs respond to changes in external flow acceleration (associated with corresponding changes in external flow pressure) [2]. A simple interpretation would be that CNs sense information regarding pressure gradients, while SNs sense the velocity of the surrounding flow. From another perspective, SNs respond best to the dc (direct current) and low-frequency components (less than approximately 30 Hz) of the incoming flow, whereas CNs respond best to high-frequency components of the flow (approximately 30–150 Hz) [3]. The lateral line organ is

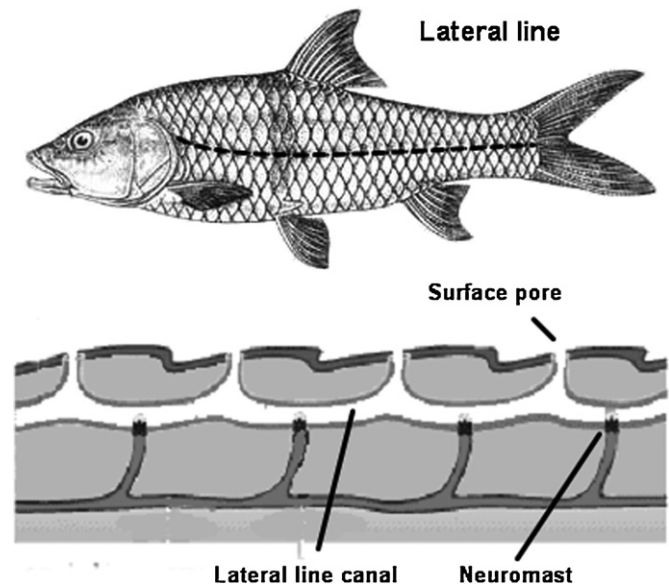


Figure 1. A schematic of LLTC and canal structure.

capable of diverse sensing tasks, ranging from the detection of near field motion [4] produced by prey [5], predators [6] or during schooling [7] to the perception of water currents and static obstacles [8]. Although individual behavioral roles of SNs and CNs have not been well distinguished, it has been found that SNs control rheotaxis at low current velocities [9], whereas CNs control the orienting response of fish to the initial prey detection [3]. It is believed that CNs are important for fish schooling [10].

In hydrodynamic studies of the lateral line, models using potential flow theory have been proposed to find the pressure distribution on a fish's skin in the presence of a stimulus. In potential flow theory, the fluid's viscosity is neglected; thus, the boundary conditions around a solid body require only that the velocity normal to the wall be equal to the wall's velocity. The potential flow model serves to approximate the pressure outside the boundary layer. This pressure essentially equals the pressure on the body's surface, because the pressure across the thickness of a thin boundary layer can be accurately approximated as being constant [11]. Consequently, potential flow is a fair model as long as the study is confined to CNs that respond to pressure gradient. The potential dipole source flow equations have been used to model a vibrating sphere near a fish's body [12]. The same equations were used by Kroese to compute the slip velocity along the fish's skin caused by a nearby vibrating sphere [13]. Potential flow around a three-dimensional slender body with circular cross-section has been obtained by Handelsman and Keller [14]. Hassan adapted this solution to investigate the cases of fish moving in open water, gliding toward a plane's surface [15], gliding alongside or above a plane's surface [16], and near an oscillating sphere [17]. Various stimuli sensed by the lateral line have been the subject of many research investigations over the years. These stimuli usually involve a vibrating sphere, moving objects, an approaching wall and vortices [18–23]. In this paper, we specifically consider Karman vortex street sensing. We will develop a model of the lateral line sensing and show that

measurement in such a model provides enough information to detect the most important parameters of such a vortex street, namely the vortex strength, the lateral and flow wise spacings, translational velocity and the orientation of the vortex street.

The ability of a fish to detect vortices by its lateral line has been demonstrated in experiments [24, 25]. Franosch *et al* [26] followed the method used by Hassan [15–17] to model the flow due to a three-dimensional vortex ring next to the fish's body. Their results showed that information about the orientation of a vortex ring is encoded in the input of the lateral line, and thus is accessible to the nervous system. Barbier has studied numerically the two-dimensional flow field due to a vortex street behind a prism [27]. He also investigated the three-dimensional flow inside the LLTC in the presence of the hair cells. However, he studied the flow in a subsegment between two adjacent pores but did not consider this internal flow over the entire length of the canal. Because of openings along the canal, internal flow velocity is expected to be non-uniform, which suggests that the distribution of velocity along the LLTC may contain rich information on external flow. The purpose of this study is to investigate the information captured by the LLTC in the presence of a Karman vortex street and to determine the relevance of this for schooling behavior. Potential flow theory is used to create a two-dimensional model of the external flow field created by a gliding fish, and the pressure distribution along the fish's surface is calculated accordingly. The internal flow inside the canal is also modeled analytically to calculate the velocity distribution along the LLTC. Finally, this information is inverted in order to determine how the original flow parameters may be gleaned from the local data available to a fish. A preliminary result from our group in this direction was presented in [28].

## 2. Theoretical modeling

In this section, a fish's body is approximated by a flat plate, and a two-dimensional potential flow model is presented to determine the pressure field around this body next to a vortex street, after which an analytical model is developed to characterize the flow inside the LLTC. For simplicity, this model is one-way coupled, meaning that the flow inside the LLTC is driven by the external flow with no feedback from internal to external flow. That is an acceptable assumption, considering the higher viscosity of the fluid inside the canal and small pore sizes which results in a very low Reynolds number flow inside the canal.

### 2.1. External flow field modeling

In potential flow theory, an infinite single row of vortices with separation  $l$  and strength  $\Gamma$  has a complex potential

$$\begin{aligned} W(z) &= \phi + \psi i = \frac{\Gamma}{2\pi i} \sum_{n=-\infty}^{+\infty} \ln(z - nl) \\ &= \frac{\Gamma}{2\pi i} \ln \sin\left(\frac{\pi z}{l}\right). \end{aligned} \quad (1)$$

The wake of an obstacle or a swimming animal is generally in the form of a Karman vortex street, which is a staggered

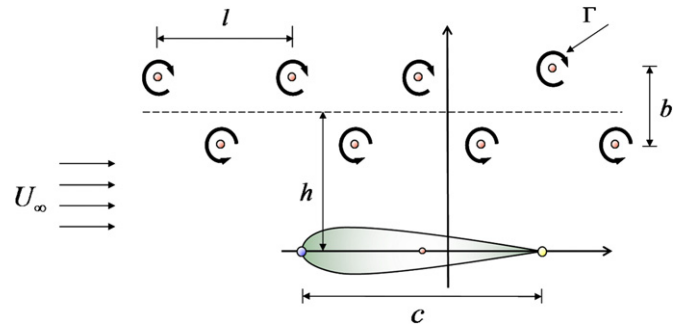


**Figure 2.** A schematic drawing of parameters governing the flow field considered in this investigation. A fish-like body in a background uniform flow superimposed on a Karman vortex street.

arrangement of two vortex rows with opposite orientations. With the vertical spacing between two vortex rows denoted by  $b$ , the stability analysis on this vortex street indicates that the ratio  $b/l$  has a constant value of about 0.28. Accordingly, the vertical distance between vortices is kept at  $b = 0.28l$  in the present study. In a static fluid, such a double-layered vortex street moves itself at an induced velocity  $u_{tr}$  which is a function of the vortex street properties as given by

$$u_{tr} = -\frac{\Gamma}{2li} \cot\left[\frac{\pi}{l}(l/2 + bi)\right] = \frac{\Gamma}{2li} \tan\left(\frac{\pi bi}{l}\right). \quad (2)$$

Here, the sign of  $\Gamma$  is determined by the upper vortex street. Superposing a free stream velocity, the total velocity of this vortex street becomes

$$\begin{aligned} u_s &= U_\infty + u_{tr} = U_\infty - \frac{\Gamma}{2li} \cot \pi (0.5 + 0.28i) \\ &= U_\infty + \frac{0.3536\Gamma}{l}. \end{aligned} \quad (3)$$

At this point, we introduce a fish in this background flow. We will consider two simplifying cases. In the first case, the fish is modeled as a simple flat plate. While this is simplistic, it is a reasonable model for fish with a low thickness-to-length ratio. As will be shown shortly, the case of the flat plate in a vortex street background flow can be solved analytically. This is quite helpful in order to understand the role of each parameter in the overall flow. For a more realistic presentation of a fish, what we call a *fish-like body* in the following sections, we will present a two-dimensional fish by a symmetrical airfoil. As a boundary layer forms around the fish's body in the presence of a free stream, its surface approximates a straight line parallel to the fish's body [29]. As noted earlier, the pressure predicted by the potential flow outside the boundary layer is equal to the pressure inside the boundary layer. For simplicity we assume that this flat body lies along the  $x$  axis of the complex  $z$ -plane with a Karman vortex street parallel to one side of the fish's body; see figure 2. In order to make the body surface streamlined, the method of images is used by introducing another vortex street on the other side of the body, so that the flow field is symmetric about the  $x$  axis. The complex potential of such a flow field can be written as

$$\begin{aligned} W(z, t) &= U_\infty z \\ &+ \frac{\Gamma}{2\pi i} [\ln \sin A - \ln \sin B - \ln \sin C + \ln \sin D], \end{aligned} \quad (4)$$

where

$$A = \frac{\pi}{l} [z - u_s t + 0.5l - i(h + 0.14l)], \quad (5)$$

$$B = \frac{\pi}{l} [z - u_s t + 0.5l + i(h + 0.14l)], \quad (6)$$

$$C = \frac{\pi}{l} [z - u_s t - i(h - 0.14l)], \quad (7)$$

$$D = \frac{\pi}{l} [z - u_s t + i(h - 0.14l)]. \quad (8)$$

Here  $A$ ,  $B$ ,  $C$  and  $D$  terms indicate the locations of the four vortex trains. The complex velocity is then given by the derivative of the complex potential,  $W$ , to be

$$u - vi = \frac{\partial W}{\partial z} = U_\infty + \frac{\Gamma}{2li} [\cot A - \cot B - \cot C + \cot D]. \quad (9)$$

On the body's surface, where  $z = x + 0i$ , the velocity normal to the body's surface should be zero, namely  $v|_{z=x} = 0$ . Thus, we have the surface velocity

$$V_{\text{surf}} = u|_{z=x} = U_\infty + \frac{\Gamma}{2li} [\cot A - \cot B - \cot C + \cot D]_{z=x}. \quad (10)$$

Owing to the symmetry of the flow field, the stream function on the body equals zero and this value does not change over time. As a result, the complex potential,  $W$ , on the body is a real-valued function which equals the velocity potential,  $\phi$ . Accordingly, the time derivative of the complex potential is also a real-valued function

$$\begin{aligned} \left. \frac{\partial W}{\partial t} \right|_{z=x} &= \left. \frac{\partial \phi}{\partial t} \right|_{z=x} \\ &= \frac{\Gamma u_s}{2li} [-\cot A + \cot B + \cot C - \cot D]_{z=x}. \end{aligned} \quad (11)$$

Bernoulli's equation can be employed in order to obtain a pressure distribution  $P$  along the fish's body

$$P_{\text{surf}} = \left[ P_0 - \frac{1}{2} \rho V_{\text{surf}}^2 - \rho \frac{\partial \phi}{\partial t} \right]_{z=x}. \quad (12)$$

Here,  $P_0$  is the total pressure at the far field. For convenience, we let  $P_0 = \frac{1}{2} \rho U_\infty^2$ . Substituting (3), (10) and (11) into (12), one obtains the following equation for the pressure distribution along the fish's body:

$$\begin{aligned} P_{\text{surf}} &= \frac{\rho \Gamma^2}{8l^2} (\cot A - \cot B - \cot C + \cot D)^2 \\ &\quad + \frac{0.3536 \rho \Gamma^2}{2l^2 i} (\cot A - \cot B - \cot C + \cot D). \end{aligned} \quad (13)$$

The created pressure gradient along the body of the fish is the driving force behind the flow inside the LLTC. For simplicity, we assume that the pressure on the canal openings is determined only by the external flow and not affected by the flow inside the canal, meaning that the outside and inside flows are one-way coupled.

## 2.2. Model of the flow inside the canal

In the previous section, we obtained the pressure distribution on the body's surface. In order to predict the response of hair cells inside the canal to this external pressure, a model of the flow inside the canal is required. In this study, the canal is modeled as a long, slender circular pipe with

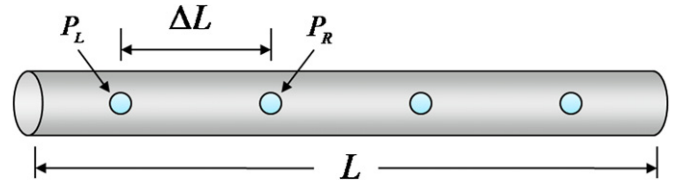


Figure 3. A schematic drawing of our model of a canal lateral line.

pores uniformly distributed along the surface of the pipe at certain intervals (see figure 3). For simplicity, the presence of hair cells inside the canal is not considered in the flow calculations. While the morphological characteristics of the trunk lateral line neuromasts vary across different species, averaged common values are used for several parameters in our model. Consequently, the diameter of the pipe,  $d$ , is taken to be  $250 \mu\text{m}$ , the diameter of each pore,  $d_p$ , to be  $250 \mu\text{m}$  and the interval between two adjacent pores,  $\Delta L$ , to be  $4 \text{ mm}$  [30]. Because the fluid inside the canal is more viscous than that outside [31] and the diameter of the canal is small, the Reynolds number for flow is much smaller than 1. As a result, the governing momentum equation of this flow simplifies to Stokes' linear equation.

The flow inside the canal is driven by the pressure gradient between adjacent pores. The linearity of the governing equation allows one to consider the flow in each segment separately. Previous computational results indicate that the value of the pressure at a cross section of the canal located at the pore is essentially the external pressure at that opening [27]. Therefore, the pressure on the body's surface where the canal openings are located determines the flow inside the canal.

For an infinitely long and periodic vortex street passing a fish, a periodic pressure wave is expected at each pore location. Accordingly, the pressure gradient between adjacent pores can be expanded in terms of a Fourier series. Here, the case of cosinoidal pressure difference is considered, namely

$$P_L - P_R = |P_L - P_R| \cos \omega t, \quad (14)$$

where  $P_L$  and  $P_R$  are the pressures at the left and right ends of the pipe, respectively.  $|P_L - P_R|$  and  $\omega$  are the wave amplitude and angular frequency, respectively.

Flow driven by a periodic pressure gradient inside a circular pipe of diameter  $d$  and length  $\Delta L$  has been investigated before by analytical techniques [32]. As the kinematic Reynolds number  $\omega_D^* = \omega(d/2)^2/\nu < 4$ , where  $\nu$  is the kinematic viscosity of the fluid inside the pipe, the induced velocity in the pipe is in phase with the pressure oscillation. The flow velocity  $u_{\text{in}}$  of the fluid inside the pipe, written in cylindrical coordinates, is given by

$$\begin{aligned} u_{\text{in}}(r) &= \frac{K}{4\nu} [(d/2)^2 - r^2] \cos \omega t \\ &= \frac{1}{4\mu \Delta L} [(d/2)^2 - r^2] (P_L - P_R), \end{aligned} \quad (15)$$

where

$$K = |P_L - P_R|/\rho \Delta L, \quad (16)$$

and  $\rho$  and  $\mu$  are the density and dynamic viscosity of fluid inside the canal, respectively. We digress here to discuss the validation of this assumption. A small  $\omega_D^*$  can be obtained,

as long as the oscillation frequency of the pressure gradient is low. Since the viscosity,  $\nu$ , of the fluid inside the canal is approximately five times that of water [31], the assumption of  $\omega_D^* < 4$  is satisfied as long as the frequency is below 200 Hz. The exact frequency limit for the validity of this assumption changes slightly with the canal diameter and fluid viscosity inside the canal which both vary from one species of fish to another. For the pressure gradient created by a vortex street, it can be shown that this stimulus contains only low-frequency components and hence the model applies for this specific case. For an arbitrary stimulus that changes in time, however, the model only applies to its low-frequency components. In other words, the model is valid for stimuli of which the leading components are within the frequency limitation. Nevertheless, the stimuli detected by fish are often in the low-frequency range [33].

According to equation (15), the amplitude of the velocity inside the canal is proportional to the pressure gradient between two adjacent pores, and the change of velocity is in phase with the pressure oscillation. For simplicity, here we assume that the spacing of adjacent pores is infinitely small so that the pressure gradient  $dp/dx$  could be approximated by  $\Delta p/\Delta L$ . In this sense, the flow velocity distribution inside the canal is assumed to be driven by a continuous pressure gradient. The validation of this assumption and its produced errors will be discussed in a later section.

The local flow velocity inside the canal is characterized by the mean flow velocity over the cross-sectional area of the canal. By substituting (13) into (15) in the limit of  $\Delta L \rightarrow 0$  and averaging over  $r$ , one obtains

$$V_{in} = \bar{u}_{in} = \frac{\pi d^2 \Gamma^2}{128 \nu l^3} (-\cot^2 A + \cot^2 B + \cot^2 C - \cot^2 D) \times (\cot A - \cot B - \cot C + \cot D - 0.77072i). \quad (17)$$

For simplicity, no interactions between the inside flow and the neuromasts are considered here, but one can expect the local flow velocity to be detected by hair cells located between adjacent pores. As has been shown by van Netten, the combined frequency response of the canal and neuromast results in a nearly constant sensitivity to pressure gradient for frequencies up to approximately 100 Hz [34]. This enables us to neglect the frequency response of the system, since the problem considered here is in the low-frequency range.

Up to this point, we have derived an analytical expression of the inside flow velocity that is related to the external flow field. Yet this equation needs to be nondimensionalized in order to understand the effect of each variable.

### 2.3. Nondimensionalization

There are nine parameters involved in the velocity equation (17) inside the canal. These are

$$\begin{array}{cccccccc} U_{\infty} & V_{in} & \Gamma & x & l & h & d & t \\ [LT^{-1}] & [LT^{-1}] & [L^2T^{-1}] & [L] & [L] & [L] & [L] & [T] \\ \nu & & & & & & & \\ [L^2T^{-1}] & & & & & & & \end{array} \quad (18)$$

The dimension of each variable is shown in brackets. Using the Buckingham  $\Pi$  theorem, one can write the expected functional relationship as

$$\pi^* = U_{\infty}^{a_1} V_{in}^{a_2} \Gamma^{a_3} x^{a_4} l^{a_5} h^{a_6} d^{a_7} t^{a_8} \nu^{a_9}. \quad (19)$$

Considering that the rank of the coefficient matrix is 2, one expects seven independent nondimensional numbers. In the following, we use  $l$  and  $U_{\infty}$  as the proper length and velocity scales for nondimensionalization. These seven nondimensional numbers are

$$\begin{aligned} x^* &= \frac{x}{l}, & h^* &= \frac{h}{l}, & d^* &= \frac{d}{l}, & \Gamma^* &= \frac{\Gamma}{U_{\infty} l}, & V^* &= \frac{V_{in}}{U_{\infty}}, \\ t^* &= \frac{U_{\infty} t}{l}, & \nu^* &= \frac{\nu}{U_{\infty} l}. \end{aligned} \quad (20)$$

Accordingly, the dimensionless internal velocity equation is

$$V^* = \frac{\pi (d^* \Gamma^*)^2}{128 \nu^*} (\cot^2 A - \cot^2 B - \cot^2 C + \cot^2 D) \times (\cot A - \cot B - \cot C + \cot D - 0.7072i), \quad (21)$$

with

$$A^* = \pi [x^* + (0.71\Gamma^* - 1)t^* + 0.5 - i(h^* + 0.14)], \quad (22)$$

$$B^* = \pi [x^* + (0.71\Gamma^* - 1)t^* + 0.5 + i(h^* + 0.14)], \quad (23)$$

$$C^* = \pi [x^* + (0.71\Gamma^* - 1)t^* - i(h^* - 0.14)], \quad (24)$$

$$D^* = \pi [x^* + (0.71\Gamma^* - 1)t^* + i(h^* - 0.14)]. \quad (25)$$

As seen,  $A^*$ ,  $B^*$ ,  $C^*$  and  $D^*$  terms are functions of  $\Gamma^*$ ,  $x^*$ ,  $h^*$  and  $t^*$ . At the initial time  $t^* = 0$ , these terms reduce to

$$A_0^* = \pi [x^* + 0.5 - i(h^* + 0.14)], \quad (26)$$

$$B_0^* = \pi [x^* + 0.5 + i(h^* + 0.14)], \quad (27)$$

$$C_0^* = \pi [x^* - i(h^* - 0.14)], \quad (28)$$

$$D_0^* = \pi [x^* + i(h^* - 0.14)]. \quad (29)$$

We now recast equation (21) to its nondimensional form to read

$$\frac{128 V^* \nu^*}{\pi (d^* \Gamma^*)^2} = (\cot^2 A_0^* - \cot^2 B_0^* - \cot^2 C_0^* + \cot^2 D_0^*) \times (\cot A_0^* - \cot B_0^* - \cot C_0^* + \cot D_0^* - 0.7072i). \quad (30)$$

Now defining a rescaled velocity

$$\Pi =: \frac{128 V^* \nu^*}{\pi (d^* \Gamma^*)^2} = \frac{128 \nu V_{in} l^3}{\pi d^2 \Gamma^2}, \quad (31)$$

equation (30) can be reduced to

$$\Pi = g_0(x^*, h^*). \quad (32)$$

From this equation, one can see that the contribution of  $\Gamma$ ,  $l$  and  $d$  to the inside velocity is simply to scale its amplitude uniformly along the canal, while the general shape of the velocity distribution along the canal is given by  $\Pi = g_0(x^*, h^*)$ . This dimensionless function is plotted in figure 4. Since, for each  $h^*$ , the velocity profile is determined uniquely by (32) up to a scaling factor, one may think of  $h^*$  as a parameter which controls the characteristic features (e.g., locations of peaks and troughs) of the velocity profile.

We now turn our attention to equation (21) in order to investigate the time dependence as the vortex street translates with respect to the fish. Since the effect of increasing  $t^*$  is equivalent to increasing  $x^*$ , the shape of the velocity plot does not change as the vortex street moves in time,  $t^* > 0$ , and it moves downstream at the same speed as the vortex street  $u_s$ .

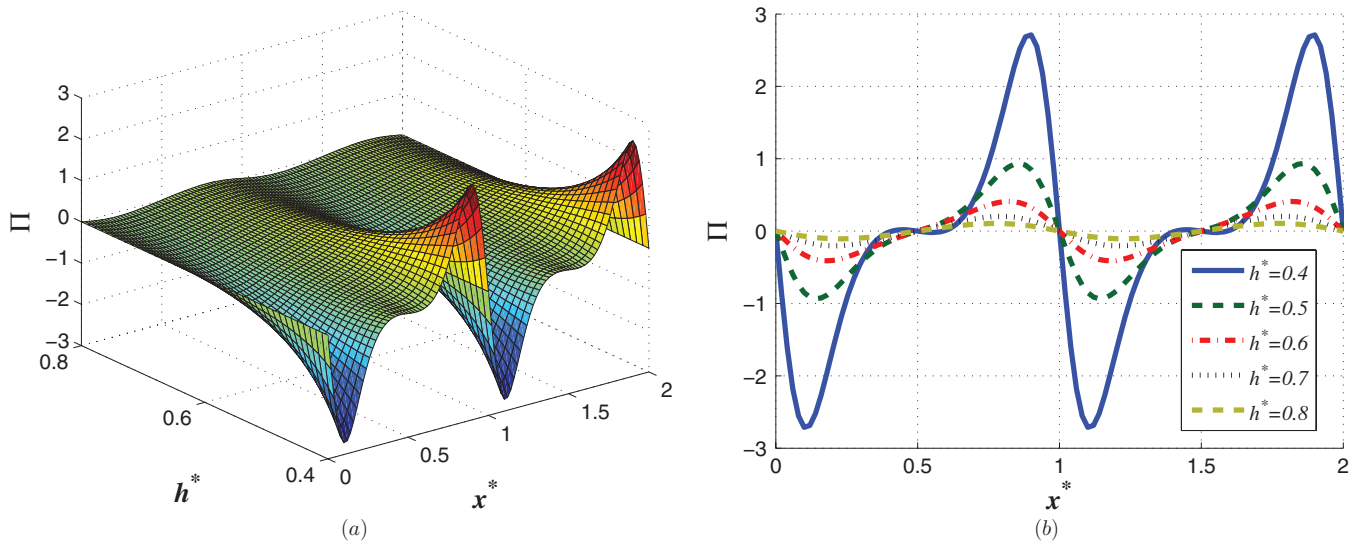


**Figure 4.** (a) The surface plot of  $\Pi = g_0(x^*, h^*)$ . (b) The plot of  $\Pi = g_0(x^*, h^*)$  as a function of  $x^*$  for several values of  $h^*$ . Since the inside flow velocity is proportional to  $\Pi$ , the shape of the curve is essentially the velocity distribution along the entire canal.

2.4. Analytical results for a flat body

In the previous section, we investigated the qualitative dependence of each dimensionless variable to the velocity distribution along the canal. This velocity distribution is driven by the differential pressure at the pores which represent the external pressure outside a thin boundary layer. To this end, one might hypothesize that a fish senses the flow inside its lateral line canal without direct knowledge of the external velocity field. This is in contrast to SNs where it is believed that the external velocity field is directly measured. It is of interest to see how much information can potentially be retrieved by a fish if it is able to precisely measure the flow velocity inside the lateral line canal. In this section, we will study the possibility of recovering these variables once the velocity distribution inside the canal is measured.

The main parameters identifying a vortex street are the vortex strength,  $\Gamma$ , the streamwise spacing between vortices,  $l$ , the distance between the vortex street and the body,  $h$ , and the velocity of the vortex street,  $u_s$ . According to the analytical solution given by equation (17), the flow velocity inside the canal is a function of these variables. As previously seen in equations (31) and (32), the amplitude of the velocity inside the canal is controlled by  $\Gamma$ ,  $l$  and  $d$ , while the dependence of the velocity on  $x^*$  and  $h^*$  is captured by the function  $g_0(x^*, h^*)$ . This function has a periodicity of 1, inherited by the periodicity of the problem.

As shown in figure 4, the features of  $\Pi = g_0(x^*, h^*)$  plot along the  $x^*$  axis change as the value of  $h^*$  is varied. Consequently, one may expect to be able to calculate  $h^*$  from these changes. For small values of  $h^*$ , a near-flat section is found between a positive peak and a negative trough. As  $h^*$  increases, this section degenerates and eventually disappears around  $h^* = 0.5$ . Besides small shifts in the locations of the peaks and troughs, no visible qualitative change in features of the scaled velocity  $\Pi$  is observed for constant  $h^* > 0.5$ . The distance between adjacent peaks and troughs is found to depend exclusively on  $h^*$ . This conclusion can also be verified

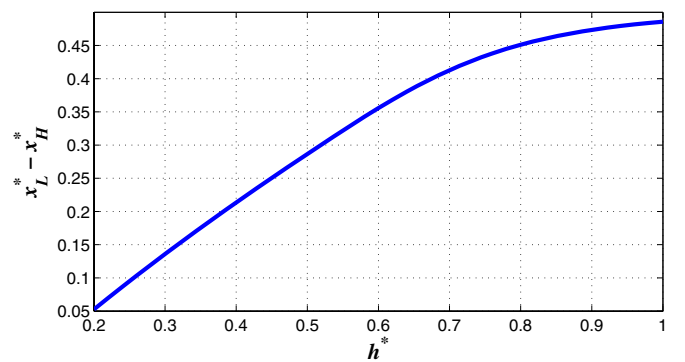


**Figure 5.** The distance between an adjacent peak and trough versus the dimensionless number  $h^*$ .

by analyzing the analytical solution. The  $x^*$  locations of the peaks and troughs of the function  $g_0(x^*, h^*)$  can be determined by

$$\frac{\partial g_0(x^*, h^*)}{\partial x^*} = 0. \tag{33}$$

This calculation results in two roots, namely  $x_H^* = h_1(h^*) + n$  and  $x_L^* = h_2(h^*) + n$  ( $n = 1, 2, 3, \dots$ ), which represent the locations of the peaks and troughs, respectively. Therefore, the distance between an adjacent peak and trough can be calculated to be  $x_L^* - x_H^* = h_2(h^*) - h_1(h^*)$ . This relation is shown in figure 5. As the value of  $l$  is easily determined from the mean velocity distribution inside the canal, the value of  $h$  is simply obtained by  $h = h^*l$ .

Now, assume that a fish can measure the velocity magnitude  $V_{in}$  inside the canal at the location of the hair cells. As discussed before, a fish is able to determine  $h^*$  from the measured velocity inside the canal. It also has access to information on the dimensionless velocity  $\Pi$  at the same location through the functional relation of  $\Pi$  to  $h^*$  and  $x^*$ .

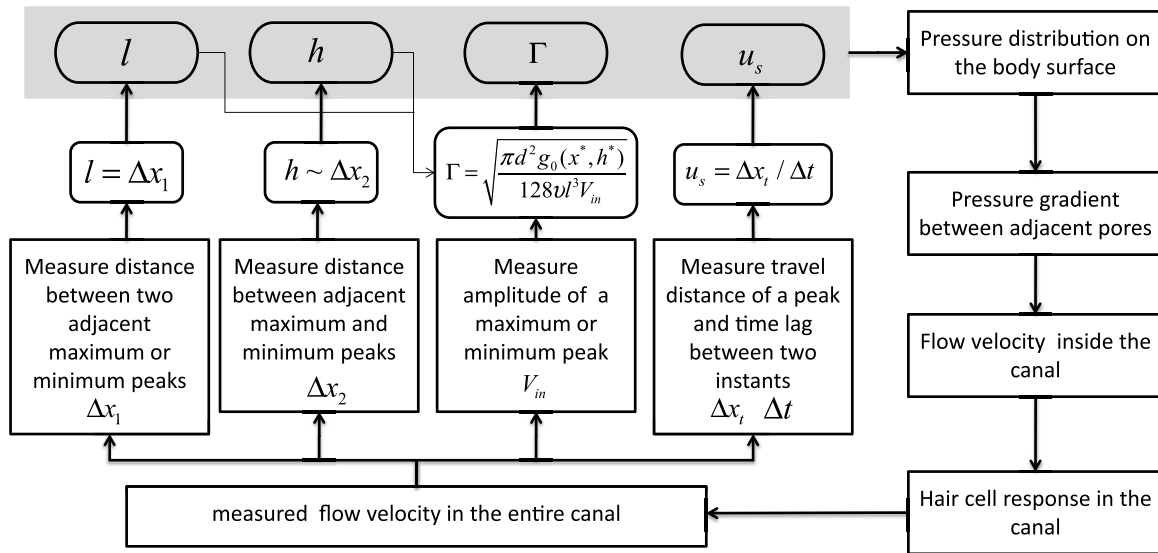


**Figure 6.** A flow chart showing the process of recovering the parameters of a vortex street from a measured velocity distribution inside the LLTC.

Therefore, a fish has enough information to calculate the strength of the vortices in a vortex street from

$$\Gamma = \sqrt{\frac{\pi d^2 \Pi}{128 \nu V_{in} l^3}}, \quad (34)$$

where the canal diameter,  $d$ , and the viscosity of fluid inside the canal,  $\nu$ , are known for a given fish.

The translation of a vortex street outside the fish’s body is accompanied by a similar periodic variation in the measured velocity inside the canal. As a result, the velocity  $u_s$  of the vortex street is essentially the rate of motion of the sensed velocity peaks inside the canal. Therefore, one can imagine that a fish detects  $u_s$  by detecting the distance traveled by the sensed peak or trough velocity during a certain time period.

So far we have developed an analytical solution for the flow around a fish represented by a 2D flat surface in the presence of a vortex street. We were also able to show that there is enough sensed information in an LLTC to recover all of the main parameters of a vortex street. A summary of our discussion for detecting these parameters is shown in figure 6. In order to extend this analytical analysis from a flat plate to a fish-like body in the presence of a vortex street, a few of the steps need to be conducted computationally. This will enable us to investigate the effect of body thickness on the sensing capabilities of an LLTC. This is presented in the following section.

### 3. Numerical method for fish-like body

#### 3.1. Joukowski transformation

In this section, we approximate the shape of a fish by a symmetric airfoil. In order to take advantage of some of our theoretical findings from the previous section, we restrict this study to the realm of potential flow theory. The shape of a fish’s body can be obtained using a Joukowski transformation [35]. The flow over a cylinder of radius  $a$  located at a point  $(c_0 - a, 0)$

can be mapped onto a symmetric airfoil (see figure 7), namely a fish-like body, by

$$z = \zeta + \frac{c_0^2}{\zeta}. \quad (35)$$

The chord length,  $c$ , and the thickness,  $\delta$ , of the body are then determined by

$$c = 2c_0 - [(c_0 - 2a) + c_0^2 / (c_0 - 2a)], \quad (36)$$

$$\delta = \frac{3\sqrt{3}}{2}(a - c_0). \quad (37)$$

The Karman vortex street is modeled by placing two rows of staggered, periodic 2D vortices on one side of the airfoil. We are not able to obtain a simple closed form analytic formulae for this case. As a result, we model the infinite array of vortices by including enough terms in the series so that the value of velocity potential difference at a specific surface point, after one cycle of the finite vortices moving downstream, is less than 0.5% of the initial potential value. In this sense, the resulting flow field near the body is a good approximation to the infinite vortex street case. The locations of the point vortices are first determined in the  $z$ -plane, and then their corresponding locations in the  $\zeta$  plane are calculated according to the inverse Joukowski transformation. Solving the inverse Joukowski transformation ( $z$  to  $\zeta$  coordinate mapping) in equation (35) for  $\zeta$  results in a multi-valued solution

$$\zeta = \frac{1}{2}(z \pm \sqrt{z^2 - 4c_0^2}). \quad (38)$$

The implication of this function is that there are two possible  $\zeta$  coordinates in the cylinder frame ( $\zeta$ -plane) for each  $z$  coordinate in the airfoil frame ( $z$ -plane). One of the  $\zeta$  coordinates is outside the cylinder and the other is inside the cylinder. Therefore, in order to properly map a  $z$  coordinate to the appropriate  $\zeta$  coordinate, the following condition is applied in order to ensure that the mapped area is outside the cylinder. The  $\zeta$  coordinate corresponding to a given vortex located at a  $z$  coordinate will be the solution in equation (38) if the distance

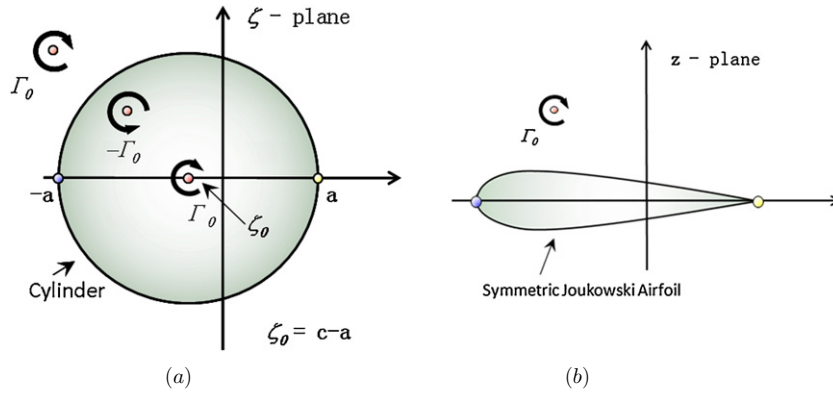


Figure 7. The flow field before and after Joukowski transformation.

to the center of the circle is greater than the radius of the cylinder ( $|\zeta| > a$ ). In this case, the inverse transform remains single valued. For  $|\zeta| = a$ , the positive imaginary solution of equation (38) is chosen.

As vortices are placed outside the cylinder in the  $\zeta$ -plane, a set of image vortices are introduced inside the cylinder in order to preserve the shape of the cylinder [36]. The complex potential in this case can be finally written as

$$W(\zeta) = U_\infty \left[ \zeta + \frac{a^2}{\zeta} \right] + \frac{i\Gamma}{2\pi} \sum_{n=1}^N \left[ \ln(\zeta - \zeta_0) + \ln(\zeta - \zeta_n) - \ln \left( \zeta - \zeta_0 - \frac{a^2}{\bar{\zeta}_n - \zeta_0} \right) \right], \tag{39}$$

where  $\zeta_0$  is the center of the cylinder and  $\zeta_n$  is the coordinate of each vortex with its complex conjugate denoted by  $\bar{\zeta}_n$ . The real part of the above function is the velocity potential  $\phi$ . The flow velocity on the body surface can be determined as the gradient of this function on the fish's body surface, that is,

$$U(z) = \left[ \sqrt{\left( \frac{\partial \phi}{\partial x} \right)^2 + \left( \frac{\partial \phi}{\partial y} \right)^2} \right]_{z=z_0}. \tag{40}$$

Assuming a quasi-steady flow, the velocity potential around the fish at any instant of time can be modeled by the 2D potential in equation (39). In order to obtain the pressure distribution around the fish's body,  $P(z)$ , we employ the Bernoulli equation

$$\left[ \frac{P(z)}{\rho} + \frac{1}{2}U^2(z) + \frac{\partial \phi}{\partial t} \right]_{z=z_0} = P_0, \tag{41}$$

where  $P_0$  is the total pressure at the far field. Just as with our analytical model in the previous section, here we let  $P_0 = \frac{1}{2}\rho U_\infty^2$  for convenience. Once we have computed the external pressure distribution, we may continue to use the same analytical model presented in the previous section to calculate the flow inside the canal. The results of this numerical model are discussed in the next sections in comparison with the results from our analytical calculations for a flat-body object.

### 3.2. Effects of body thickness

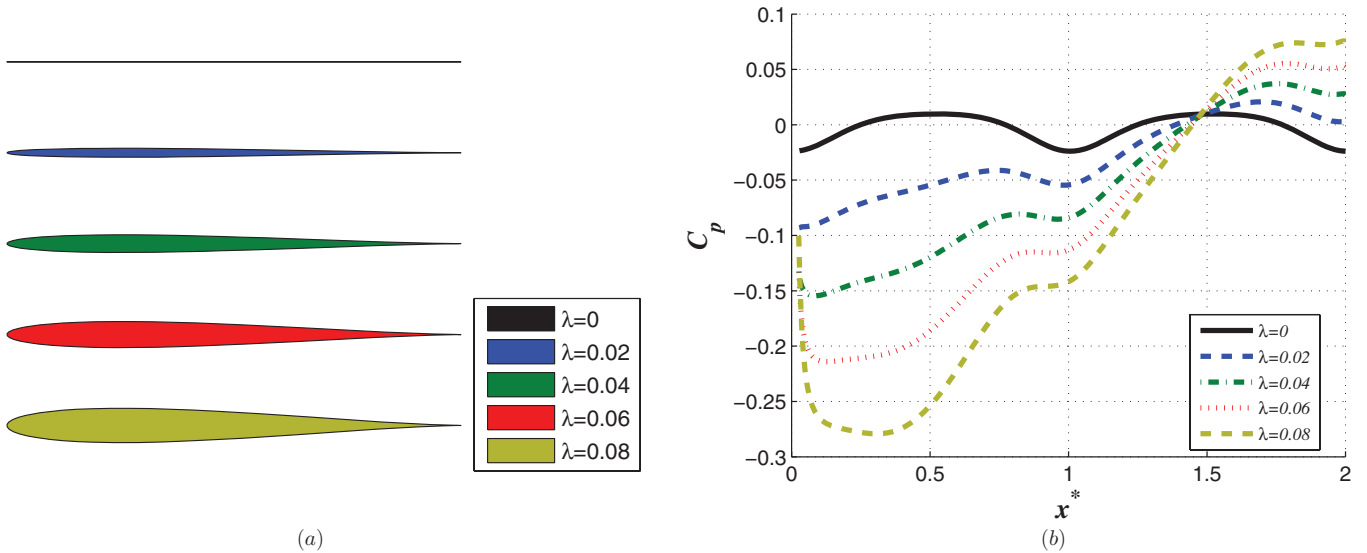
To evaluate the accuracy of the numerical method, we consider the flow around a flat-body object as a test case. A flat-body

object could be considered as the limit of a fish-like body from the previous section when the body thickness approaches zero. In this case we will be able to compare our numerical procedure with the exact analytical result for a flat-body object. In order to evaluate the effect of body thickness, we define the thickness ratio, as illustrated in figure 8(a), to be body thickness over body length

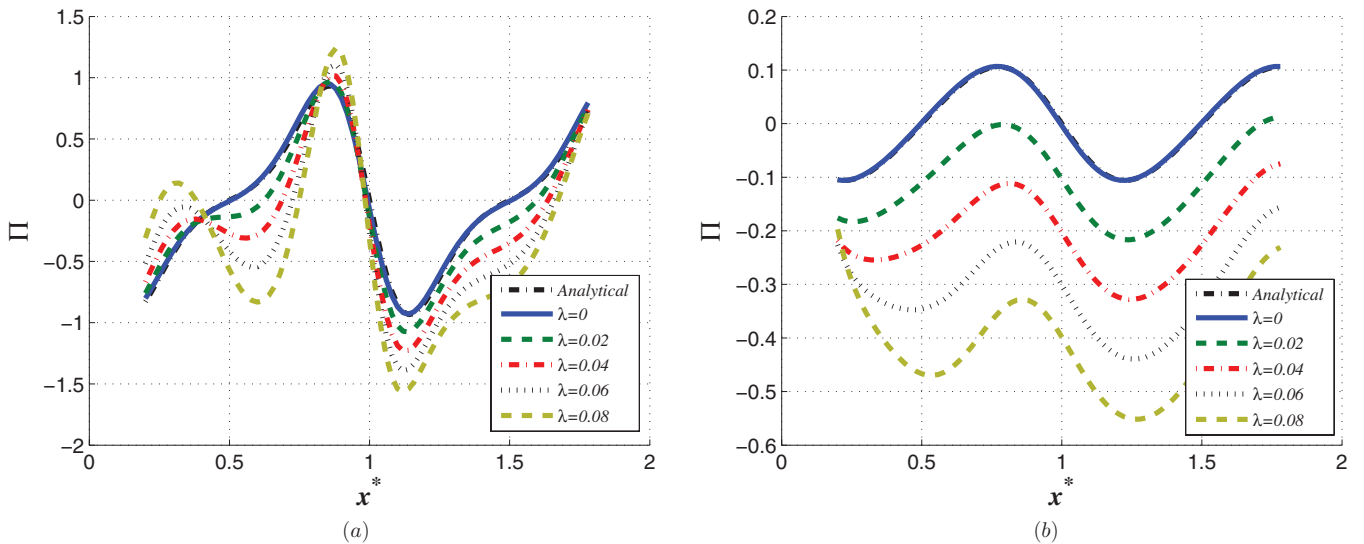
$$\lambda = \delta/c. \tag{42}$$

Figure 8(b) shows the variation in the pressure distribution as  $\lambda$  is changed from a flat plate to a relatively rounded fish body with  $\lambda = 0.08$ . For larger  $\lambda$  when the fish's body is rather bluff, a sharp drop in pressure along the body is observed as one moves away from the stagnation point on the fish's head. After that initial drop, pressure gradually increases along the body toward the tail. By increasing the thickness ratio, the pressure around the head region will be dominated by the stagnation pressure, which is dictated by the incoming free stream. The existence of a vortex street hardly alters the pressure distribution in this region. Since the induced velocity in the canal is proportional to the external pressure gradient, the inside velocity in this region does not contain much information on the vortex street. Also based on the fact that the LLTC often does not extend to the fish's head, in this study we assume that the LLTC ranges from  $0.1c$  to  $0.9c$  along the fish's body.

For convenience, the value of  $l$  is measured in the cord length,  $c$ , units. The variable with a star is still scaled by  $l$  as previously defined. The data shown in figure 9(a) use the same  $\lambda$  values as before with  $c^* = 2$ ,  $h^* = 0.5$  and  $\Gamma^* = 0.6$ . For smaller values of  $h^*$ , where the vortex street moves closer to the fish's body, a secondary positive peak-velocity appears on the left side of the absolute peak-velocity value by increasing the value of the thickness ratio  $\lambda$ . The adjacent locations of the peak and trough velocities move closer to each other by a small distance, and the amplitude evidently increases especially at the negative trough. It seems that the enhanced surface curvature in a fish-like body tends to amplify the peaks and troughs in the velocity curve. It should be noted that these features, created by the external vortices in the velocity distribution, are much more distinct than the features of the velocity induced by the pressure distribution due to the body curvature in a uniform flow. Therefore, one might consider the



**Figure 8.** (a) Drawing of fish-like bodies with thickness ratios,  $\lambda$ , ranging from 0 to 0.08. (b) The pressure distribution along the body surface.  $C_p$  is the pressure coefficient defined as  $C_p = P/\frac{1}{2}\rho U_\infty^2$  with  $c^* = 2$ ,  $h^* = 0.5$  and  $\Gamma^* = 0.6$ . The results of four bodies with thickness ratios of  $\lambda = 0.02, 0.04, 0.06$  and  $0.08$  are shown in comparison with that of a flat body with  $\lambda = 0$ .



**Figure 9.** A plot of the dimensionless velocity inside the canal,  $\Pi$ , along the LLTC. Four bodies with thickness ratios of  $\lambda = 0.02, 0.04, 0.06$  and  $0.08$  are shown in comparison with a flat body. (a)  $c^* = 2, h^* = 0.5$  and  $\Gamma^* = 0.6$ ; (b)  $c^* = 2, h^* = 0.8$  and  $\Gamma^* = 0.6$ .

effect of the canal on the flow signal as of a differential filter. For larger values of  $h^*$ , the features of the velocity distribution move slightly in the downstream direction for increasing body thickness values; see figure 9(b). Aside from this phase shift, the velocity plot maintains its main features, meaning that the relative locations of the velocity peaks and troughs are rather unchanged. For  $\lambda = 0.04$  and higher, some perturbations in the velocity profile are observed around the fish's head where the surface curvature is maximum. Because the fish's posterior body is fairly similar to a flat plate, the features of the inside velocity distribution in this region are rather unchanged as compared to the flat-body case (see also figure 4(b)). Similar to the analytical results for a flat body, the value of  $l$  can be determined as the distance between two corresponding peaks or troughs as demonstrated in figure 10. In addition,

the variations in  $l$  do not change the general features of the inside velocity distribution, as seen in figure 11.

Figure 12 demonstrates the effect of varying the vortex strength. The dimensionless number  $\Gamma^*$  does not change the overall features of the velocity distribution inside the canal, but it could change the amplitude of the velocity peaks. This observation also agrees with our analytical result in the previous section for a flat body. Inspired by the definition of  $\Pi$  in our analytical model, we further consider a dimensionless number  $\Pi \Gamma^{*2}$  instead of  $\Pi$ . The result indicates that the amplitudes of  $\Pi \Gamma^{*2}$  at peaks and troughs fit a quadratic polynomial with respect to  $\Gamma^*$ ,

$$\Pi \Gamma^{*2} = a_1 \Gamma^{*2} + a_2 \Gamma^* + a_3, \quad (43)$$

where  $a_1, a_2$  and  $a_3$  are functions of  $l$  and  $h$ . Since  $l$  and  $h$  may be determined by sensed information available to a fish, these

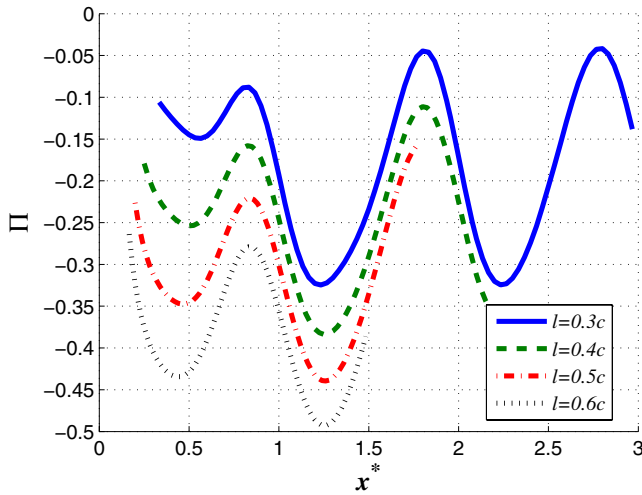


**Figure 10.** The plot of the dimensionless velocity inside the canal,  $\Pi$ , as a function of location along the LLTC for several values of  $l$  with  $h^* = 0.8$ ,  $\Gamma^* = 0.6$  and  $\lambda = 0.06$ . The distance between two corresponding peaks remains almost constant. That is,  $\Delta x^* \approx 1$ .

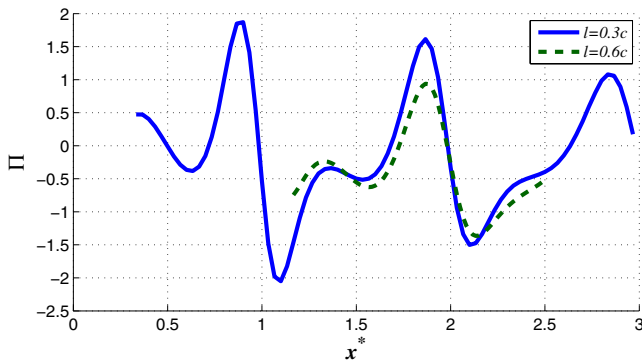
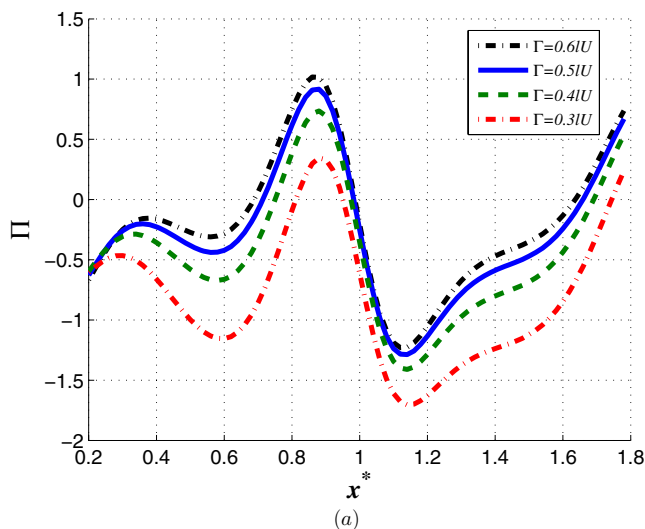


**Figure 11.** A comparison of the dimensionless velocity inside the canal,  $\Pi$ , between two values of  $l$  with  $h^* = 0.5$  and  $\Gamma^* = 0.6$ . Note that the curve corresponding to  $c^* = 5/3$  is shifted one period along the  $x^*$  axis for comparison.



coefficients can also be calculated from the sensed data. If a fish is able to measure the velocity inside the LLTC,  $\Pi$ , then it can deduce the strength of the vortices,  $\Gamma^*$ , in an incoming vortex street from the amplitude of the velocity peaks as shown in figure 12(b).

Having determined the effects of  $\Gamma^*$  and  $l$  on the velocity distribution inside the LLTC, one can conclude that, for a given fish's body,  $h^*$  had a dominant effect on changing the features of the velocity distribution inside the LLTC. The value of  $h^*$  can again be evaluated by detecting the distance between consecutive maximum and minimum points in  $\Pi$ , similar to the flat-body case. It should be noted that as a vortex street is shifted away from the fish's body, say that  $h^*$  exceeds a threshold value  $h_c^*$ , the influence of the vortex street on the velocity inside the canal is diminished and the canal velocity will only be influenced by the pressure created by the free stream flow passing the body; see figure 13. On this view, the fish with a larger thickness ratio has less sensitivity to measure the vortex street at a greater distance, because its body induces a larger pressure gradient which could overwhelm information of other stimuli at a greater distance.

### 3.3. Vortex street on one side of the body

In our analytical model, we introduced vortex streets on both sides of the fish's body in order to preserve the streamlined fish-like body in our theoretical solution. Yet, the case with a vortex street on one side of the body is actually more pertinent. This can easily be done by employing the numerical technique in the previous section. This result is shown in figure 14. As one can expect, there is no significant difference between vortices on only one side and vortices on both sides of the body, since the vortices on one side of the body have little influence on the near-body flow of the other side. Only the velocity near the body's head and tail is altered. In this sense, all the conclusions drawn in the previous sections could be carried over to the case of a fish with a vortex street on one

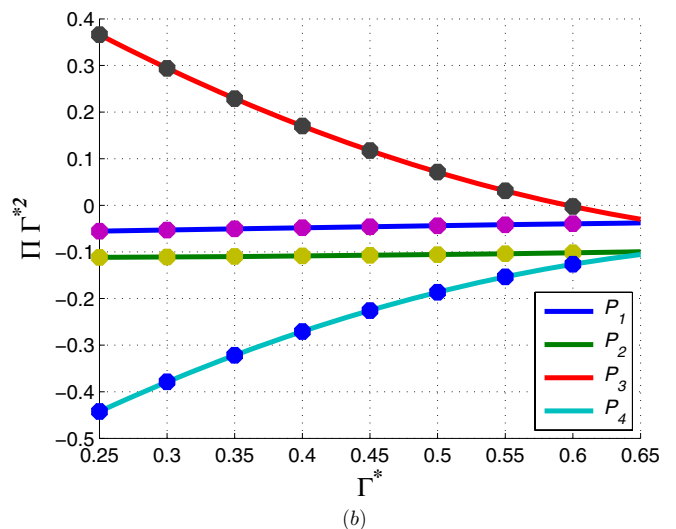


**Figure 12.** (a) The Plot of the dimensionless velocity inside the canal,  $\Pi$ , versus  $x^*$  for several values of  $\Gamma^*$  with  $c^* = 2$ ,  $h^* = 0.5$  and  $\lambda = 0.04$ . The amplitude of the peaks changes with  $\Gamma^*$ , while the main features of the velocity distribution remain unchanged. (b) The amplitude of  $\Pi \Gamma^{*2}$  at peaks and troughs ( $P_1, P_2, P_3, \dots$ ) fits in a quadratic polynomial with respect to  $\Gamma^*$ .

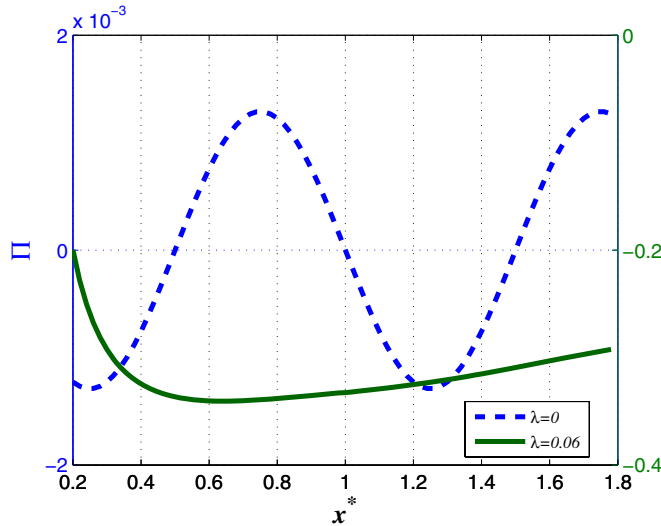


**Figure 13.** The plot of the dimensionless velocity inside the canal,  $\Pi$ , for  $h^* = 1.5 > h_c^*$  with a flat body  $\lambda = 0$  and a fish-like body with  $\lambda = 0.06$ . Peaks and troughs indicating the vortex street are overwhelmed by the background flow in the fish-like body case.

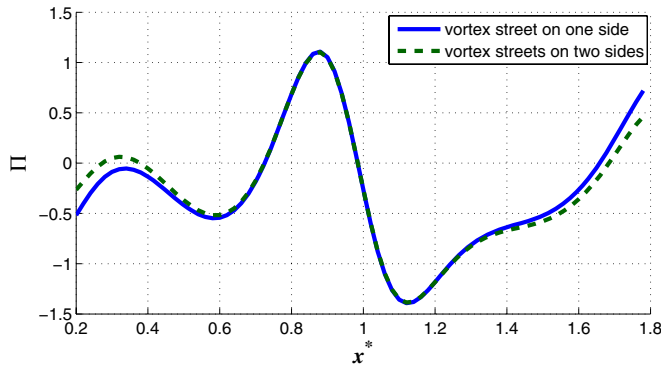


**Figure 14.** A comparison of the dimensionless velocity inside the canal,  $\Pi$ , between a vortex street on one side and vortex streets on both sides of the body.

side. This, once again, matches with our analytical results for the case of a flat-body.

It is also of interest to consider a more complex case where the vortex street axis is not parallel to the fish's body axis. Assume that the angle between the vortex street axis and the fish's body is  $\theta$ . The velocity distribution inside the LLTC for several values of  $\theta$  is shown in figure 15. The first negative trough, which is near the body's head, becomes more distinct as  $\theta$  increases, while the secondary negative trough degenerates due to the departure of vortices. The presented results could be interpreted as if the whole velocity curve is rotated along with the vortex street. To this end, this might provide enough information to a fish in order to determine the angle of an incident vortex street with the fish's body.

#### 4. Discussion

In this investigation we considered modeling the LLTC of a fish in a uniform background flow with a vortex street. A simplified model of a vortex street is constructed if one knows the

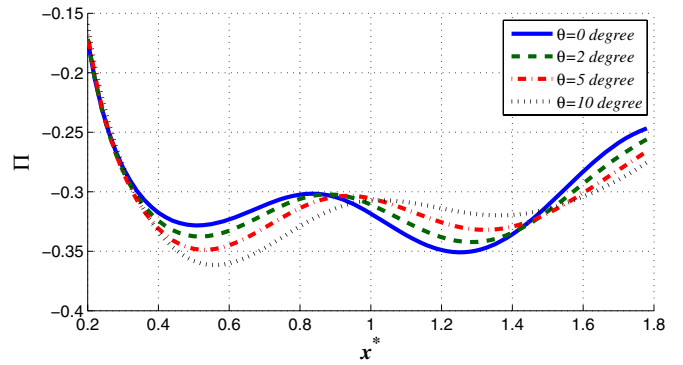


**Figure 15.** The plot of the dimensionless velocity inside the canal,  $\Pi$ , for several values of the angle  $\theta$  between the vortex street and the body.  $\lambda = 0.03$ ,  $c^* = 2$ ,  $h^* = 0.5$  and  $\Gamma^* = 0.6$ .

following parameters: the vortex strength,  $\Gamma$ , the streamwise spacing between vortices,  $l$ , the distance between the vortex street and the body,  $h$ , and the velocity of the vortex street with respect to the fish,  $u_s$ . While the velocity of the vortex street,  $u_s$ , can be easily determined by monitoring the peak or trough velocities inside an LLTC, sensing or calculation of the other parameters of a vortex street requires information on the velocity distribution throughout the entire lateral line canal of the fish. To this end, accurate sensing of the velocity inside the LLTC, information about the spacing between the pores and the overall length of the canal are all quite important for processing this information. Equation (17) for the velocity inside the LLTC shows that  $V_{in}$  is scaled with  $d^2$  and  $1/\nu$ . Therefore, one could expect that fish evolved in an environment with a low level of hydrodynamic activity, which favors evolving a more sensitive sensing organ, will have a larger canal diameter than those inhabiting a more hydrodynamically active environment. This observation matches the measured data from [37]. It should point out that, as noted earlier, it is also desired to keep a small kinematic Reynolds number  $\omega_D^*$  for the flow inside the canal such that the velocity changes in phase with the external pressure oscillation; otherwise the inside flow velocity would exhibit a more complex profile, which may impede the determination of the external pressure gradient.

An interesting observation from our LLTC modeling is that while the sensory system of LLTC provides enough information for detecting all the relevant parameters of an incoming vortex street, it is not able to detect the mean incoming velocity  $U_\infty$ . This is an interesting result and consistent with observations by others [33] that an LLTC filters out the dc (direct current) component of an incoming velocity signal. To this end, it would be interesting to see whether a fish evolved to have more lines of SNs shows the same signal filtering characteristics. Furthermore, is there any environmental reason for this lack of sensitivity to the dc component of a velocity signal? Can a line of SNs be used to detect the parameters of a vortex street?

Our LLTC model consists of two parts: (i) predicting the pressure gradient along the body of a fish and (ii) modeling a sensed velocity inside the LLTC based on this pressure gradient. While the second part (ii) is not applicable to a line of

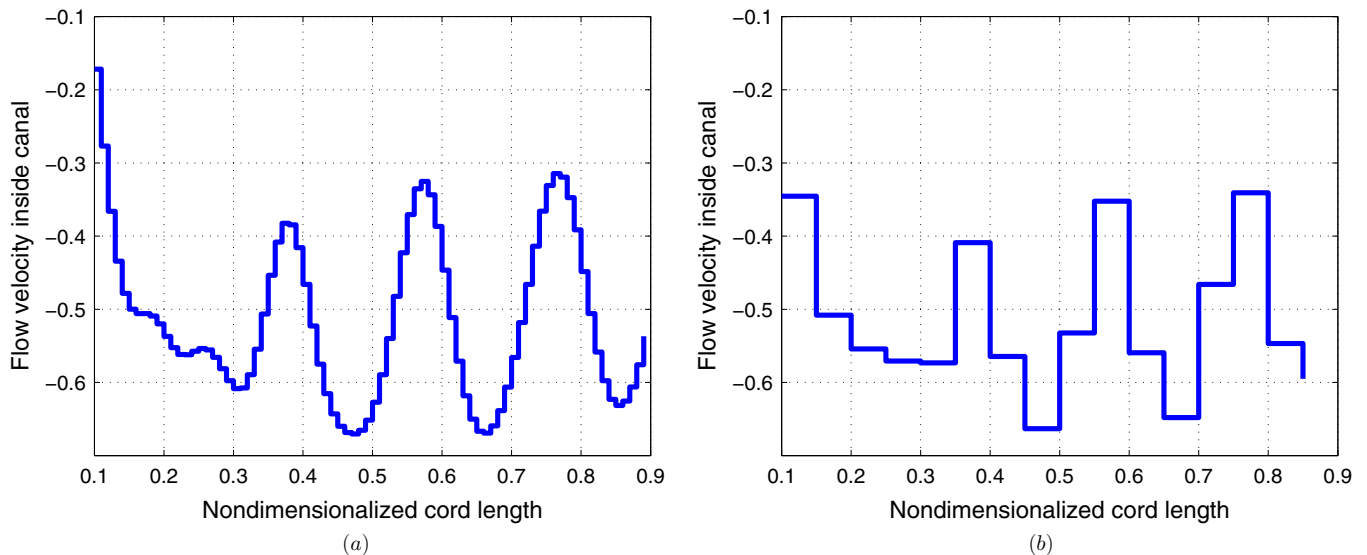


**Figure 16.** The flow velocity inside an LLTC with different pore spacings. (a)  $\Delta L = 0.01c$ . (b)  $\Delta L = 0.05c$ .

SNs, the first part (i) is still valid and applicable. Therefore, one can still use equation (10) as a model to obtain an estimate for the surface flow velocity outside the boundary layer using a line of SNs. If the free stream velocity  $U_\infty$  is much larger than the surface-induced velocity by the rest of the terms representing a vortex street, the response of the SNs will be dominated by this term and it will not be sensitive to perturbations by the vortex street. In contrast, the LLTC sensing system filters out this dc component and only processes the signal from the vortex street. As a result, our model predicts that a fish with an LLTC is more sensitive in detecting a vortex street and its parameters than a fish with a line of SNs.

In the previous sections, the flow velocity inside the LLTC was calculated to be proportional to the gradient of the external pressure along the fish's body. This is based on the assumption that the pressure can be measured with an infinitely high spatial resolution. However, in reality the spatial resolution of this detection is dictated by the pore spacing  $\Delta L$ . Any pressure gradient changes over a distance smaller than this value may not be detected by the LLTC. In order to detect a vortex street, the spacing of the pores of an LLTC should be smaller than the characteristic length of the incident vortex street. Figure 16 shows the effect of the pore spacing,  $\Delta L$ , on the sensed velocity inside the LLTC. A typical pore spacing for the LLTC of fish is about 0.01 times of the body length. The pressure gradient recorded by such a canal has a fairly good spatial resolution. As pore spacing increases, the spatial resolution is decreased and as a result some of the more detailed features of the surrounding flow field could be lost during the measurement. This has also been observed by Fernandez *et al* [38] in their studies on a linear pressure sensor array for identifying small objects. They concluded that the pressure sensor array should have a sensor-to-sensor spacing of less than 0.03 times of the sensing body length. One can imagine that if the streamwise period of the Karman vortex street is less than the pore spacing, that is,  $l < \Delta L$ , a fish would have a very hard time in detecting a vortex street. On the other hand, the length of the LLTC also determines how much information regarding the vortex street

can be obtained. It is evident that a longer LLTC would be helpful to collect more information on the surrounding flow field. An LLTC with small overall length, on the other hand, requires latency to experience the changes in the surrounding flow field as it passes over the fish. If the overall length of the LLTC is larger than the wavelength of the incident flow, the parameters of the incident vortex street could be detected from instantaneous measurements along the LLTC. On the other hand, detection of signals with wavelengths larger than the overall length of the LLTC, while possible, requires a longer detection sensing period and more processing. Therefore, an ideally fast LLTC sensing system should have its pore spacing much smaller than the characteristic length of the signal to be detected (e.g. its wavelength) and it should have a total length greater than the wavelength of the incident flow. Thus, the ratios of  $\Delta L/l$  and  $L/l$  are of importance for the sensitivity of the LLTCs of fish. This result may account for the generally small pore spacings found in most fish, and for the fact that the LLTC stretches nearly all the way along a fish's body.

The results of our study may also be used to explain some other fish behaviors, for instance, schooling behavior. It has been demonstrated that a blind fish is still able to school and to monitor the swimming speeds and directions of other fish in the school using its LLTC [7]. To this end, it is believed that a fish utilizes its LLTC sensing system to detect a vortex street wake by other fish in the school. Many fish schooling observations show that the preferred distance to the nearest neighbor for schooling fish is about one body length [10]. Considering the school structure, the vortex street shed by an anterior fish is 0.5 times the fish's body length, that is,  $h = 0.5c$ . The vertical vortex spacing,  $b$ , could be approximated by the tail-beating amplitude, which is estimated by  $0.1c-0.21c$  according to Wolfgang *et al* [39]. The downstream spacing of vortices  $l$  is then determined to be around  $0.4c-0.75c$  by the stability requirement of a Karman street  $b/l \approx 0.28$ . Accordingly, the dimensionless number  $h^*$  is in the range of  $0.7c-1.25c$ , which is well below the critical distance  $h_c^*$ , meaning that the vortex street shed by anterior fish can be detected by the LLTC.

If a fish in a school swims at a lower speed than that of its anterior neighbors, the relative speed of the vortex street with respect to the fish's body,  $u_s$ , increases. Furthermore, it is expected that an accelerating anterior fish in a school creates a vortex street with larger vortex spacing and strength, marked by an increased  $l$  and  $\Gamma$ . Another fish following this accelerating fish is then expected to sense these changes (increased  $l$  and  $\Gamma$ ) in the vortex street and thus to react appropriately to catch up to the speed of the school. On the other hand, if the anterior fish changes its direction, such a change will also alter the velocity distribution inside the LLTC, as discussed in the previous section. Again, the LLTC provides enough information to a fish in a school about the changes in the swimming direction for the anterior fish. In summary, our model demonstrates that an LLTC can provide enough information to a fish in a school in order to maintain its direction and speed with its neighboring fish.

A vortex street, shed by a large fish, is expected to have large distances between consecutive shed vortices. As discussed before, the LLTC of a smaller fish is not ideally suited for detecting such a vortex street instantly. On the other hand, if a vortex street is shed by a much smaller fish, the vortices' strength is relatively small. Therefore, the detecting fish must be sufficiently close to the wake in order to be able to sense such a vortex street. This suggests that fish are especially sensitive to the wakes created by other fish of a similar length.

## 5. Conclusions

In this paper, we developed an analytical model for the flow field around a two-dimensional fish in proximity to a vortex street. This model is used to calculate the pressure distribution on the body surface. An analytical model for the LLTC of a fish is also developed to correlate the inside canal flow velocity to the external flow field. Nondimensional parameters governing the flow detection are also identified. Our model demonstrates the effects of each dimensionless number for a flat-bodied fish. The properties of a vortex street can be theoretically determined from the sensed velocity distribution inside the canal. A strategy is proposed to determine the properties of an outside vortex street, once a velocity distribution inside the LLTC is sensed. We also developed a numerical model to validate the result of our analytical model and to extend our investigation to the case of a fish-like body. The results of this numerical model show that the velocity distribution retains similar features to that of a fish with a small thickness ratio. Consequently, a similar technique to the one we developed for a flat-bodied fish is applicable here to identify the parameters of a vortex street from velocity measurements inside the LLTC. Therefore, our model provides a framework on how a fish might identify the parameters and characteristics of a wake including its speed, amplitude of vortices, spacing of vortices, angle of the vortex street axis, etc. Such information could be used by a fish to identify the size, speed and direction of fish traveling around it. Our model also provides possible explanations on functional adaptation of the LLTC's morphology. These include the following: a lengthened canal favors information collection, reduced pore

spacing favors sensing resolution and widened canal favors sensing sensitivity. It is also argued that an LLTC could provide enough information to a fish about the direction for swimming or the accelerating/decelerating nature of the neighboring fish in a school.

## Acknowledgment

This research was supported by the Office of Naval Research.

## References

- [1] Münz H 1985 Single unit activity in the peripheral lateral line system of the Cichlid fish *J. Comp. Physiol. A* **157** 555–68
- [2] Kroese A B and Schellart N A 1992 Velocity- and acceleration-sensitive units in the trunk lateral line of the trout *J. Neurophysiol.* **68** 2212–21
- [3] Coombs S, Braun C B and Donovan B 2001 The orienting response of lake Michigan mottled sculpin is mediated by canal neuromasts *J. Exp. Biol.* **204** 337–48
- [4] Harris G G and van Bergeijk W A 1962 Evidence that the lateral line organ responds to near field displacements of sound sources in water *J. Acoust. Soc. Am.* **34** 1831–41
- [5] Bleckmann H 1980 Reaction time and stimulus frequency in prey localization in the surface-feeding fish *Aplocheilichthys lineatus* *J. Comp. Physiol. A* **140** 163–72
- [6] Pitcher T J 1993 Role of the lateral line in fish behaviour *Behaviour of Teleost Fishes* (London: Chapman and Hall) pp 201–46
- [7] Partridge B L and Pitcher T J 1980 The sensory basis of fish schools: relative roles of lateral line and vision *J. Comp. Physiol.* **135** 315–25
- [8] Hassan E S 1986 On the discrimination of spatial intervals by the blind cave fish (*Anoptichthys jordani*) *J. Comp. Physiol. A* **159** 701–10
- [9] Baker C F and Montgomery J C 1999 The sensory basis of rheotaxis in the blind mexican cave fish, *Astyanax fasciatus* *J. Comp. Physiol.* **184** 519–27
- [10] Partridge B L 1982 The structure and function of fish schools *Sci. Am.* **246** 114–23
- [11] White F M 2005 *Viscous Fluid Flow* 3rd edn (Boston, MA: McGraw-Hill)
- [12] Coombs S, Hastings M and Finneran J 1996 Modeling and measuring lateral line excitation patterns to changing dipole source locations *J. Comp. Physiol. A* **178** 359–71
- [13] Kroese A B A, Van der Zalm J M and Van den Bercken J 1978 Frequency response of the lateral-line organ of *Xenopus laevis* *Pflügers Arch.* **375** 167–75
- [14] Handelsman R A and Keller J B 1967 Axially symmetric potential flow around a slender body *J. Fluid Mech.* **28** 131–47
- [15] Hassan E S 1992 Mathematical description of the stimuli to the lateral line system of fish derived from a three-dimensional flow field analysis: I. The cases of moving in open water and of gliding towards a plane surface *Biol. Cybern.* **66** 443–52
- [16] Hassan E S 1992 Mathematical description of the stimuli to the lateral line system of fish derived from a three-dimensional flow field analysis: II. The case of gliding alongside or above a plane surface *Biol. Cybern.* **66** 453–61
- [17] Hassan E S 1993 Mathematical description of the stimuli to the lateral line system of fish derived from a three-dimensional flow field analysis: III. The case of an oscillating sphere near the fish *Biol. Cybern.* **69** 525–38
- [18] Franosch J P, Sichert A B, Suttner M D and van Hemmen J L 2005 Estimating position and velocity of a submerged moving object by the clawed frog and by fish—a cybernetic approach *Biol. Cybern.* **93** 231–8

- [19] Curcic-Blake B and van Netten S M 2006 Source location encoding in the fish lateral line canal *J. Exp. Biol.* **209** 1548–59
- [20] Goulet J, Engelmann J, Chagnaud B P, Fransoch J P, Suttner M D and van Hemmen J L 2008 Object localization through the lateral line system of fish: theory and experiment *J. Comp. Physiol. A* **194** 1–17
- [21] Sichert A B, Bamler R and van Hemmen J L 2009 Hydrodynamic object recognition: when multipoles count *Phys. Rev. Lett.* **102** 058104
- [22] Windsor S 2008 Hydrodynamic imaging by blind Mexican cave fish *PhD Thesis* University of Auckland, Auckland, New Zealand
- [23] Rapo M A, Jiang H, Grosenbaugh M A and Coombs S 2009 Using computational fluid dynamics to calculate the stimulus to the lateral line of a fish in still water *J. Exp. Biol.* **212** (Pt 10) 1494–505
- [24] Chagnaud B P, Bleckmann H and Engelmann J 2006 Neural responses of goldfish lateral line afferents to vortex motions *J. Exp. Biol.* **209** 327–42
- [25] Chagnaud B P, Bleckmann H and Hofmann M H 2007 Karman vortex street detection by the lateral line *J. Comp. Physiol. A* **193** 753–63
- [26] Fransoch L P, Hagedorn H J A, Goulte J, Engelmann J and van Hemmen J L 2009 Wake tracking and the detection of vortex rings by the canal lateral line of fish *Phys. Rev. Lett.* **103** 078102
- [27] Barbier C and Humphrey J A 2008 Drag force acting on a neuromast in the fish lateral line trunk canal: I. Numerical modeling of external–internal flow coupling *J. R. Soc. Interface* **6** 627–40
- [28] Ren Z and Mohseni K 2010 A model of lateral line of fish for vortex sensing *40th AIAA Fluid Dynamics Conf. and Exhibit* (Chicago, IL, 28 June–1 July 2010) AIAA paper 2010-4620
- [29] Windsor S P and McHenry M J 2009 The influence of viscous hydrodynamics on the fish lateral-line system *Integrative Comp. Biol.* **49** 691–701
- [30] Faucher K, Aubert A and Lagardere J 2003 Spatial distribution and morphological characteristics of the trunk lateral line neuromasts of the sea bass *Brain Behav. Evol.* **62** 223–32
- [31] van Netten S M and Kroese A B A 1987 Laser interferometric measurements on the dynamic behavior of the cupola in the fish lateral line *Hear. Res.* **29** 55–61
- [32] Uchida S 1956 The pulsating viscous flow superposed on the steady laminar motion of incompressible fluid in a circular pipe *Z. Angew. Math. Phys.* **7** 403–22
- [33] Bleckmann H 1994 *Reception of Hydrodynamic Stimuli in Aquatic and Semiaquatic Animals* (Progress in Zoology vol 41) (New York: Fischer)
- [34] van Netten S M 2006 Hydrodynamic detection by cupulae in a lateral line canal: functional relations between physics and physiology *Biol. Cybern.* **94** 67–85
- [35] Kundu P K and Cohen I M 2007 *Fluid Mechanics* (New York: Academic)
- [36] Milne-Thomson L M 1958 *Theoretical Aerodynamics* (New York: Dover)
- [37] Dijkgraaf S 1963 The functioning and significance of the lateral line organs *Biol. Rev.* **38** 51–105
- [38] Fernandez V I, Maertens A, Yaul F M, Dahl J, Lang J H and Triantafyllou M S 2011 Lateral-line-inspired sensor arrays for navigation and object identification *Mar. Technol. Soc. J.* **45** 130–46
- [39] Wolfgang M J, Anderson J M, Grosenbaugh M A, Yue D K and Triantafyllou M S 1999 Near-body flow dynamics in swimming fish *J. Exp. Biol.* **202** 2303–27